


Robust Millisecond Coherence Times of Erbium Electron Spins

Shobhit Gupta,¹ Xuntao Wu,² Haitao Zhang,³ Jun Yang,³ and Tian Zhong^{2,*}

¹*Department of Physics, University of Chicago, Chicago, Illinois 60637, USA*

²*Pritzker School of Molecular Engineering, University of Chicago, Chicago, Illinois 60637, USA*

³*Corning Research and Development Corporation, Sullivan Park, Painted Post, New York 14870, USA*

 (Received 26 July 2022; revised 27 November 2022; accepted 15 February 2023; published 10 April 2023)

Erbium-doped solids are prime candidates for quantum memories in optical quantum networks given their telecom-compatible photon emission. An electron spin of erbium with millisecond coherence time is desirable for generating remote entanglement between adjacent quantum network nodes. Here we report GHz-range electron-spin transitions of $^{167}\text{Er}^{3+}$ in a yttrium oxide (Y_2O_3) matrix with coherence times that are consistently longer than a millisecond. By polarizing paramagnetic impurity spins we achieve a spin T_2 up to 1.46 ms, and up to 7.1 ms after dynamical decoupling. These coherence lifetimes are among the longest found for erbium in crystalline matrices despite the presence of host nuclear spins. We further enhance the coherence time beyond conventional dynamical decoupling, using customized sequences to simultaneously mitigate spectral diffusion and dipolar interactions. Our study not only establishes $^{167}\text{Er}^{3+}$: Y_2O_3 as a significant quantum memory platform but also provides a guideline for engineering long-lived erbium spins in a variety of host materials for quantum technologies.

DOI: [10.1103/PhysRevApplied.19.044029](https://doi.org/10.1103/PhysRevApplied.19.044029)

I. INTRODUCTION

Rare-earth-ion dopants in solids exhibit exceptionally long spin-coherence times and narrow optical linewidths [1–3], making them a prime candidate for quantum memories and quantum transduction [4] in an optical quantum network [5], and with a good prospect for quantum sensing [6]. Kramers rare-earth ions with unpaired $4f$ electrons possess effective electron spin $S = 1/2$, and Er^{3+} in particular demonstrates telecom-wavelength optically addressable spins that are ideal for realizing quantum spin-photon interfaces in a fiber-based quantum communication network [7,8]. For such a network, the Er spin-coherence time needs to be at least a millisecond in order to efficiently generate and store entanglement over the photon transit time between adjacent network nodes, assuming a typical repeater node interval of 200 km [9]. Once generated, the entanglement between remote Er^{3+} spins can be transferred to $^{167}\text{Er}^{3+}$ nuclear spin registers for long-term storage while the electron spins are freed up for subsequent entanglement generation.

Due to large magnetic dipole moment, however, Er^{3+} electron spins experience strong decoherence from magnetic noise created by either Er^{3+} or other paramagnetic spin flip flops, limiting their coherence to the microseconds range in most prior reports [10–13]. Milliseconds Er^{3+} spin-coherence time has only been demonstrated recently

in bulk single crystals with low nuclear spin density at millikelvin temperatures: $T_2 = 1.3$ ms in 20 parts per million (ppm) doped Er^{3+} : CaWO_4 [14]; $T_2 = 23$ ms in undoped CaWO_4 [15]. Another approach to prolonging the Er^{3+} spin coherence considers $^{167}\text{Er}^{3+}$ isotope, which possesses $7/2$ nuclear spin with long-lived hyperfine transitions [2]. This gives rise to hybridized electron-nuclear spins [16,17] with zero first-order Zeeman (ZEFOZ) transitions showing reduced sensitivity to noise. Nevertheless, ZEFOZ transitions often occur at zero or low fields, where the fluctuating magnetic noise amplitude peaks due to unpolarized spin baths, and addressing them requires stringent field alignment, partially limiting the robustness of this method.

In this work, we report millisecond coherence times of electron spins of $^{167}\text{Er}^{3+}$ in a yttrium oxide host. Instead of addressing ZEFOZ transitions, we probe weakly mixed electron-spin transitions with low g factors. By freezing the impurity spins and employing customized dynamical decoupling we demonstrate consistent Er^{3+} spin-coherence time over a millisecond threshold. We investigate 20 ppm doped $^{167}\text{Er}^{3+}$ ensembles in Y_2O_3 polycrystalline hosts using electron-spin resonance (ESR) spectroscopy. Rather than host nuclear spins, we identify paramagnetic impurity spins as the primary source of decoherence. By freezing them at millikelvin temperatures, we obtain a Hahn-echo [18] coherence time of 1.46 ms, and T_2^{XY8} of 7.1 ms after dynamical decoupling (DD) of spectral diffusion. By further designing customized DD sequences to simultaneously mitigate spectral diffusion

*tzh@uchicago.edu

and instantaneous diffusion we achieve an even longer coherence than what is obtainable with conventional XY8 sequence. The strategies demonstrated in this work are applicable to a variety of host materials for erbium and other Kramers rare-earth spins, including those containing nuclear spins and paramagnetic impurities. Thus, this work provides a general recipe for engineering long-coherence rare-earth spins as appealing resources for quantum technologies.

II. EXPERIMENTAL METHODS

We use yttrium oxide (Y_2O_3) as a host matrix for $^{167}\text{Er}^{3+}$ dopants, which has been synthesized in diverse forms such as single crystals, polycrystalline ceramics, nanoparticles, and thin films [21], with ultranarrow, sub-kilohertz optical linewidths already demonstrated in Er^{3+} -doped Y_2O_3 transparent ceramics [22,23]. The sample under study is a 20 ppm $^{167}\text{Er}^{3+}$ -doped Y_2O_3 ceramics with 95% isotopic purity prepared by sintering Er^{3+} -doped Y_2O_3 nanoparticles. The average grain size is $0.90 \mu\text{m}^2$. Y_2O_3 has a cubic crystal structure (T_h^7 space group) with 16 formula units per unit cell [24,25]. These 32 Y^{3+} sites can be grouped into two classes with 24 sites of C_2 point

group symmetry [Fig. 1(a)], and 8 sites for C_{3i} point group symmetry [Fig. 1(c)], where each of the 32 Y^{3+} ions in a unit cell has been shown to be substituted with an Er^{3+} ion with an equal probability [26,27].

Er^{3+} ion has a $[\text{Xe}]4f^{11}$ configuration with $^{2S+1}L_J = ^4I_{15/2}$ ground state. In a crystal field of low symmetry the $J = 15/2$ ground state splits into eight Kramers doublets with the lowest doublet being occupied at cryogenic temperatures, leading to an effective $S = 1/2$. Erbium has five stable isotopes ($^{162,164,166,168,170}\text{Er}$) with zero nuclear spin, and a ^{167}Er isotope with $I = 7/2$ nuclear spin. The spin Hamiltonian of the lowest Kramers doublet of $J = 15/2$ manifold of $^{167}\text{Er}^{3+}$ in Y_2O_3 can be modeled as,

$$\mathcal{H} = \mu_e \mathbf{B} \cdot \mathbf{g} \cdot \mathbf{S} + \mathbf{I} \cdot \mathbf{A} \cdot \mathbf{S} + \mathbf{I} \cdot \mathbf{Q} \cdot \mathbf{I} - \mu_n g_n \mathbf{B} \cdot \mathbf{I}, \quad (1)$$

where μ_e is the Bohr magneton, \mathbf{B} is the external magnetic field, \mathbf{g} is the g -factor tensor, \mathbf{A} is the hyperfine tensor, g_n is the nuclear g factor, and \mathbf{Q} is the nuclear quadrupole tensor.

We use the principle values of g , A , and Q tensors for C_2 and C_{3i} sites obtained from a separate study [20] to calculate the spin energy levels with magnetic field as shown in Figs. 1(b) and 1(d). Due to the random orientation of

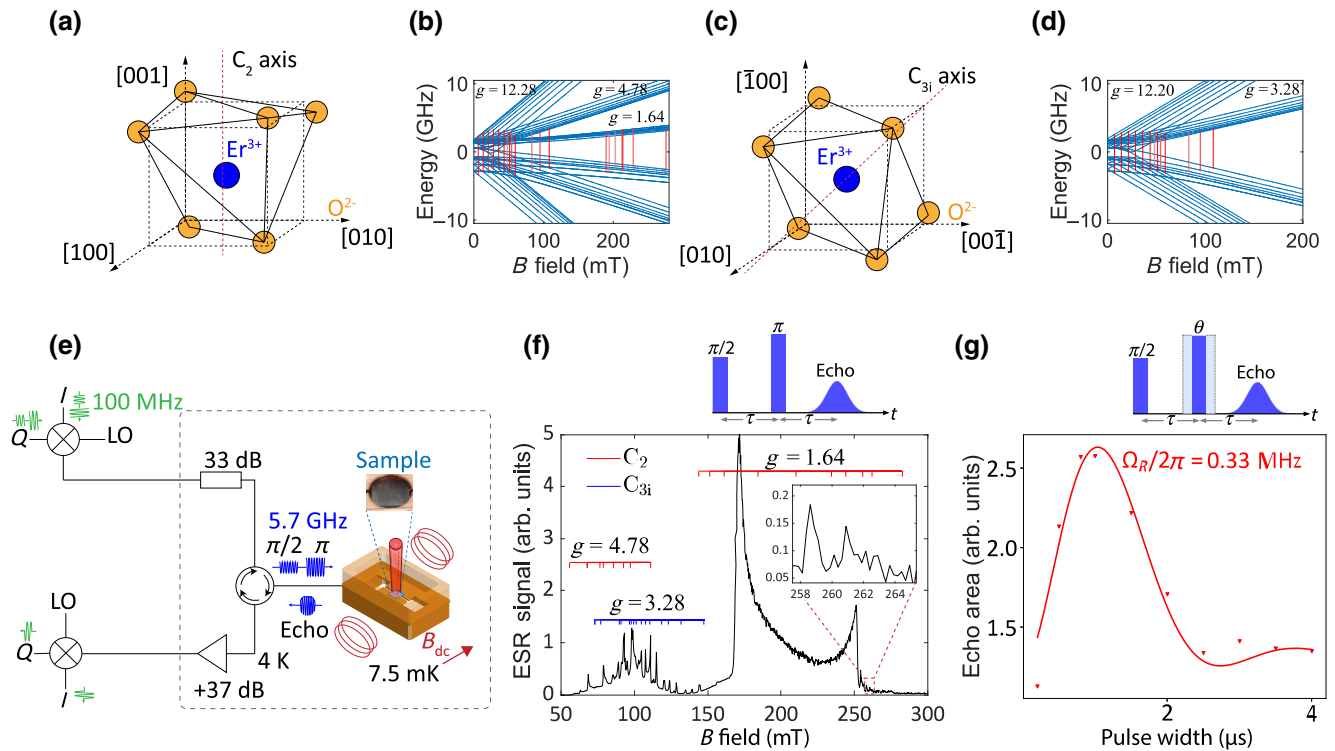


FIG. 1. (a),(c) $\text{Er}^{3+}:\text{Y}_2\text{O}_3$ crystal structure showing the unit cell and Er^{3+} substituting in C_2 and C_{3i} sites, respectively. (b),(d) Zeeman and hyperfine energy levels for $^{167}\text{Er}^{3+}$ in C_2 and C_{3i} sites, respectively, generated along the eigenaxes of the g tensors with Easypin [19]. The red lines show the allowed ESR transitions at 5.67-GHz resonance frequency. The spin energy levels and transitions in a magnetic field are discussed in detail in Ref. [20] (e) Millikelvin pulsed ESR setup. (f) Echo detected field sweep of $^{167}\text{Er}^{3+}:\text{Y}_2\text{O}_3$ showing predicted transitions as dashes grouped by their g factors. (g) Rabi nutation of echo signal obtained by varying refocusing pulse length for the transition at 259 mT. Sequences above (f),(g) show pulse amplitude in voltage.

crystal grains in a polycrystalline sample, while ESR transitions from $g = 12.2$, $g = 4.78$, and $g = 3.28$ overlap, we can individually address transitions with $g = 1.64$ in the region of 160–275 mT at approximately 5-GHz ESR frequency [Figs. 1(b) and 1(d)]. The transitions with $g = 1.64$ are of interest in this study due to their lowest sensitivity to noise, and strong coupling to microwaves given the high transverse g factor up to 12.2 [28].

We perform ESR spectroscopy on a sample with dimensions of $4.6 \times 4.6 \times 1$ mm³, which is mounted in between the two halves of a three-dimensional (3D) copper loop-gap resonator [29]. The resonator is made with oxygen-free copper and is assembled with two halves with a gap exactly matching the sample size for good thermal conduction [Fig. 1(e)]. The resonator is mounted on the mixing chamber stage of a dilution refrigerator (Bluefors LD 250) and has a 5.67-GHz resonance frequency with a loaded Q of 3500 at 7.5-mK base temperature. A three-axis vector magnet (AMI Model 430) is used to apply a dc bias field. Laser illumination is applied to the sample using an objective lens that has weak focus on the sample with approximately 2 mm beamspot size.

3D resonators offer advantages over two-dimensional (2D) superconducting microresonators for ESR, including higher field homogeneity, the ability to apply out-of-plane magnetic fields, easier integration with optics, as well as compatibility with diverse sample geometry [30]. However, reduced sensitivity of 3D resonators typically requires the use of high-power pulses (on the order of Watts) leading to heating and elevated temperatures [31] of the ESR spectrometer. We use heterodyne-detection technique along with a low-noise preamplifier (HEMT) [Fig. 1(e)] to enhance the spectrometer sensitivity, allowing for low power (on the order of 100 μ W) pulsed ESR measurements. This results in a lowest possible temperature of the sample stage of 7.5 mK during the experiment, allowing us to maximally polarize the spin population. Rabi frequency of 0.33 MHz is obtained in a two pulse echo sequence with varying refocusing (second) pulse length [Fig. 1(g)], which allows us to estimate a transverse g factor 7.5, in close agreement with the expected average transverse g factor between 4.8 and 12.2 for ensembles of crystallites with their eigenaxes having $g = 1.64$.

We note that the 0.33-MHz Rabi frequency and 1.3-MHz resonator bandwidth in our experiment are both smaller than the spin inhomogeneous linewidth of 41 MHz, which effectively suppresses spin-spin interactions by addressing a subensemble of spins. While the low effective excited spin density in our experiments is relevant to applications involving addressing single spins as well as frequency multiplexed quantum memories, the spin-spin interaction would be stronger when addressing the entire spin ensemble as required by certain memory protocols such as spin-wave atomic frequency combs [32–34]. Nevertheless, the use of low g (e.g., $g = 1.64$) transitions are

still highly advantageous in this regard as they inherently have weaker spin-spin interaction, which scales as g^2 .

To identify all ESR transitions of $^{167}\text{Er}^{3+}$, we perform echo-detected field sweep (EDFS) measurement by sending 1- μ s-long $\pi/2$ and π pulses at a separation of 5 μ s, and sweep magnetic field to detect spin echo from different transitions [Fig. 1(f)]. We observe spin echoes from $g = 4.78$, $g = 3.28$ in the < 150 mT region and $g = 1.64$ transitions extending from 160 to 275 mT, seen as a long tail in the spectra. The group of red and blue dashes in Fig. 1(f) show the ESR transitions for the crystallites with their eigenaxes of the g tensor oriented along the magnetic field. These transitions correspond to the expected peaks in the ESR spectrum of a polycrystalline sample.

III. SPIN COHERENCE AND RELAXATION TIMES

For the ESR transitions observed in Fig. 1(f), we measure spin-relaxation times, Hahn-echo coherence times, and coherence times under XY8 dynamical decoupling at the base temperature. Figure 2(a) shows T_1 (black), Hahn echo T_2 (red), and dynamically decoupled T_2^{XY8} (blue) as a function of B field. We fit the decay of integrated echo amplitudes with a stretched exponential $\exp(-2\tau/T_2)^n$, where n is the stretch factor. Figure 2(a) shows T_2 coherence times approaching or exceeding 1 ms (green dashed line) for the majority of the transitions above 100 mT, with the highest T_2 of 1.46 ms measured around 259 mT from $g = 1.64$ transitions [blue box in Fig. 2(a)]. The coherence time increases with fields due to lower sensitivity of high field (lower effective g) transitions to spectral diffusion (SD) and instantaneous diffusion (ID) [35] noise. At a 5.67-GHz splitting, the sensitivity of ESR transition to magnetic noise ($\partial E / \partial B$) is simulated to be approximately equal to $g\mu_B$ (Supplemental Material [36]), therefore electron-nuclear spin mixing does not play a significant role in the measured long coherence time [17]. The measurable lowest field transition at 70 mT showed a T_2 of 100 μ s along with a strong modulation of echo amplitudes due to superhyperfine couplings [23,37]. The stretch factor n increases from 1 for the lowest field transition (70 mT) to 2.5 for the highest field transition (270 mT), indicating spectral diffusion as a decoherence mechanism for the latter transitions [38].

Decoherence due to spectral diffusion can be suppressed with dynamic decoupling [39,40]. While Carr-Purcell-Meiboom-Gill (CPMG) sequence preserves only a specific spin state [39] and can result in an artificial elongation of the coherence times in the presence of pulse errors, XYN pulse sequences offer a robust performance against pulse errors leading to an efficient suppression of spectral diffusion close to the instantaneous diffusion limit for an arbitrary spin state [41]. Figure 2(a) shows a clear increase in coherence times from approximately 1 ms with Hahn

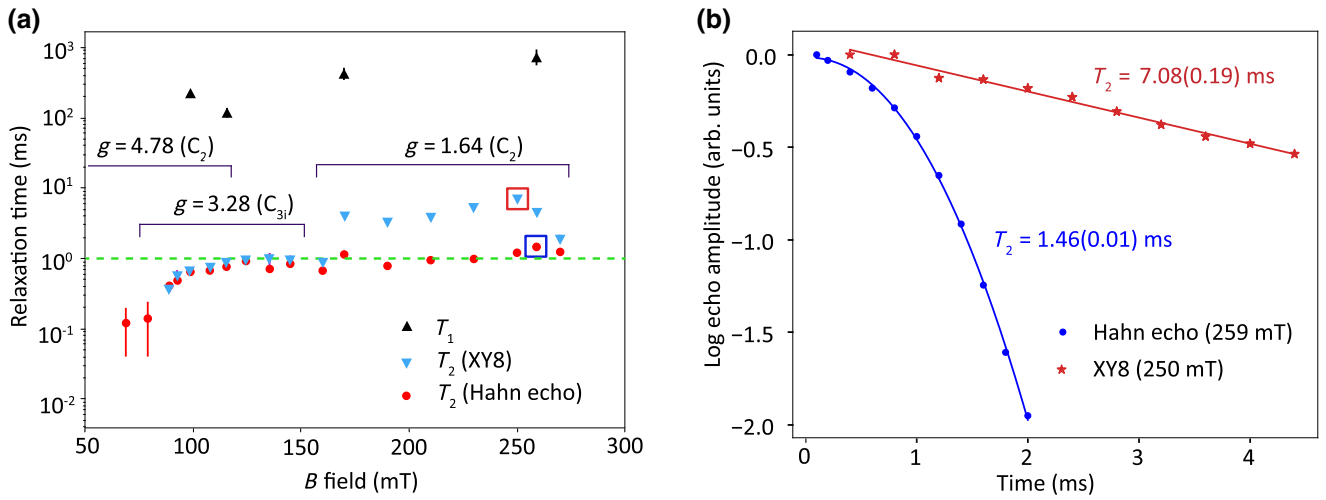


FIG. 2. Electron spin coherence and relaxation times of $^{167}\text{Er}^{3+}$: Y_2O_3 at millikelvin temperatures. (a) Spin lifetime (T_1) (black triangles) is measured using saturation recovery. Spin-coherence time measured with two pulse echo (T_2 , red dots) and with XY8 dynamical decoupling (T_2^{XY8} , blue triangles) showed coherence times exceeding 1 millisecond spin-coherence time (green dashed line) for lower g transitions. Red and blue boxes highlight the longest XY8 and Hahn-echo coherence times, respectively. (b) Echo decays for the two transitions with longest Hahn echo and XY8 coherence times, as highlighted in (a).

echo to beyond 3 ms with XY8 sequence for high-field (> 150 mT) transitions, with the longest T_2^{XY8} of 7.08 ms for the 250-mT transition (red box). The echo decays with XY8 sequence were well fitted with a single exponential decay. In this measurement, we sent $N = 248 \pi$ pulses. Further increasing N did not yield longer coherence, indicating an effective filtering of the low-frequency noise [42]. Therefore, we expect that the measured T_2^{XY8} is limited by instantaneous diffusion (ID) and possible contribution from higher frequency noise. The coherence time improvement with XY8 is less pronounced for lower field transitions, which suggests an increase in instantaneous diffusion with higher effective g factors, scaling approximately as g_{eff}^2 [43]. This explains the sharp increase in T_2^{XY8} at around 170 mT. We estimate the theoretical instantaneous diffusion limited T_2 of 9.4 ms for the $g = 1.64$ transition [blue box, Fig. 2(a)], which is in agreement with the measured T_2^{XY8} of 4 ms for the same transition, suggesting that the coherence time under XY8 sequence is ID limited (Supplemental material [36]). We also infer from this estimate that SD is dominant over ID as the decoherence mechanism. Thus we do not expect a significant degradation of coherence time as we increase the pulse power, as verified by the measurement of Hahn echo T_2 as a function of the refocusing pulse power (Supplemental Material [36]). Spin T_1 for a few transitions is also measured using saturation-recovery sequence and is found to be in the range of 100 ms to 0.7 s (Fig. 2(a) black triangles).

ESR transitions between 150–250 mT could have mixed contributions from Er and other paramagnetic impurities. Therefore, it is imperative to verify those transitions are indeed from Er spins. By illuminating the sample with a

laser pulse on resonance with the C_2 site optical transition around 1535.6 nm, we observe a clear optically modulated spin-echo signal for the ESR transition around 259 mT, which cannot be attributed to other heating effects (Supplemental Material [36]), thereby validating its assignment to $^{167}\text{Er}^{3+}$ spins in the C_2 site.

IV. DECOHERENCE AT SUBKELVIN TEMPERATURES

A. Temperature dependence of decoherence and relaxation processes

We perform temperature-dependent relaxation and coherence time measurements for the 259-mT ($g = 1.64$) transition to understand decoherence mechanisms below 1 K. We use continuous-wave off-resonant laser at 191 THz (1570 nm) to heat the sample directly. The actual sample temperature is estimated from the electron-spin echo amplitudes and by correlating it to the recorded stage temperature [31](Supplemental Material [36]). A sample temperature of 26 mK is determined based on the a spin-polarization model when the stage temperature is 7.5 mK.

The electron-spin lifetimes (T_1) measured using saturation recovery [black dots, Fig. 3(a)] show an increase from 42 ms at 0.95 K to 0.73 s at 26 mK. The spin T_1 temperature dependence for rare-earth dopants at temperature below 4 K can be modeled by a combination of direct phonon, flip-flop, and temperature-independent processes

(black line) [44],

$$\frac{1}{T_1} = R_0 + R_{\text{ff}} \text{sech}^2\left(\frac{hf}{2k_B T}\right) + R_D \coth\left(\frac{hf}{2k_B T}\right) \quad (2)$$

where R_D is the rate of direct phonon process, R_{ff} is the rate of flip-flop process and R_0 represents a temperature independent component with f being the transition frequency. The fitted coefficients are $R_D = 2.19$ Hz, $R_{\text{ff}} = 0.87$ Hz, and $R_0 = 1.67 \times 10^{-8}$ Hz.

The Hahn-echo spin-coherence times T_2 show strong dependence on temperature [Fig. 3(a)] from 58 μs at 0.95 K to 1.46 ms at 26 mK. The echo decay is fitted with a stretched exponential and exhibited a stretch factor in the range of 1.3 to 2.1, pointing to spectral diffusion as the dominant decoherence mechanism throughout the temperature range. Improvement in coherence times with XY8 dynamical decoupling [T_2 , (XY8)] in the same temperature range is also indicative of a spectral diffusion dominated decoherence [blue dots in Fig. 3(a)].

To model the temperature dependence of T_2 and to obtain spectral diffusion parameters for the environment spin bath, we consider three contributions: spectral diffusion-limited coherence time, $T_{2,\text{SD}}$, instantaneous diffusion $T_{2,\text{ID}}$ and spin relaxation limit $2T_1$, so $T_2^{-1} = T_{2,\text{SD}}^{-1} + T_{2,\text{ID}}^{-1} + (2T_1)^{-1}$. Spectral diffusion limited coherence, $T_{2,\text{SD}}$ can be modeled using a Lorentz diffusion model with a stretch factor 2 [35,43],

$$T_{2,\text{SD}}^{-1} = \frac{\sqrt{\pi} \Gamma_{\text{SD}} R}{2} \quad (3)$$

where Γ_{SD} represents the spectral diffusion linewidth due to dipolar interaction with environmental spins and R is the flip rate of the environment spins. The temperature-dependent Γ_{SD} can be modeled as [45],

$$\Gamma_{\text{SD}} = \Gamma_{\text{max}} \text{sech}^2(g_{\text{env}} \mu_B B) / (2k_B T), \quad (4)$$

where g_{env} is the effective g factor and Γ_{max} is the maximum dipolar broadening with environment spins causing spectral diffusion.

The contribution of decoherence from instantaneous diffusion $T_{2,\text{ID}}$ can be estimated from the measured coherence time after XY8 dynamical decoupling, as it represents the remaining decoherence that cannot be canceled by the XY8 sequence. If we were to assume the total flip rate $R(T)$ for the environment spin bath as the inverse of Er^{3+} T_1 from the fit (black curve) in Fig. 3(a), then by fitting the T_2 temperature dependence, we obtain spin-bath parameters $\Gamma_{\text{max}} = 2.80(0.51)$ MHz and $g_{\text{env}} = 0.70$, which are not consistent with $^{167}\text{Er}^{3+}$ spin-induced spectral diffusion. While Γ_{max} of 2.80 MHz is significantly larger than the spectral diffusion linewidth of 124 kHz due to erbium spins (Supplemental Material [36]), $g_{\text{env}} = 0.70$ is smaller

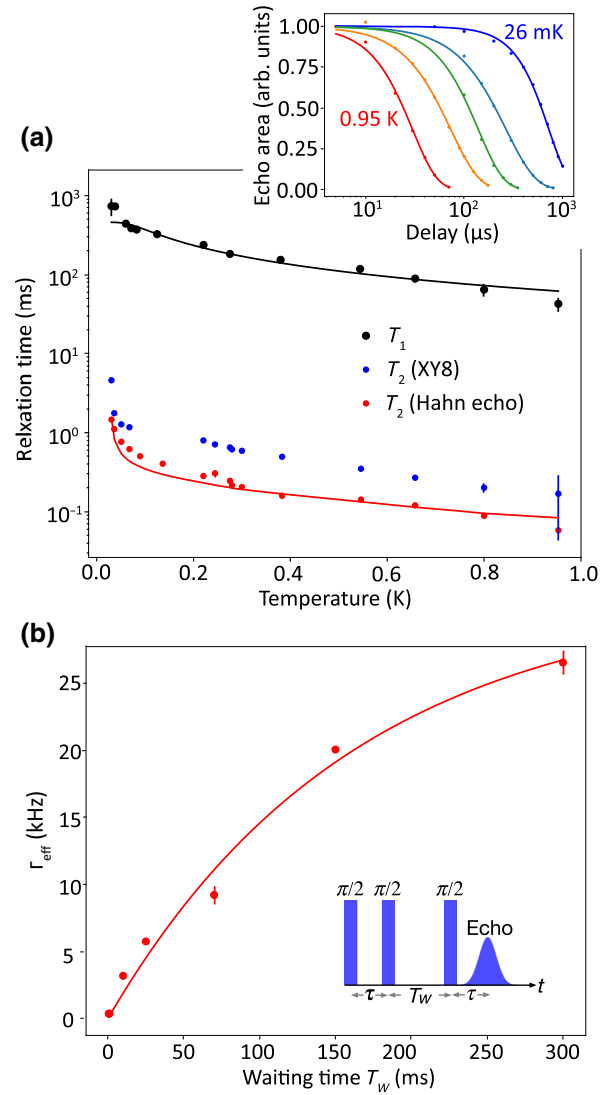


FIG. 3. Decoherence mechanisms at sub-Kelvin temperatures for the $^{167}\text{Er}^{3+}$ $g = 1.64$ (259 mT) transition. (a) Temperature dependence of relaxation and decoherence processes: spin lifetime (T_1 , black dots) fitted with Eq. (2) (black line); coherence time (T_2 , red dots) fitted with the T_2 model described in the text (red line); XY8 dynamical decoupling coherence time (T_2^{XY8}) measured by sending 30 XY8 pulses. Inset shows time-domain Hahn-echo decays for the range of temperatures measured. (b) Spectral diffusion measured with three pulse echoes at a base temperature of 26 mK.

than the lowest g (1.64) of $^{167}\text{Er}^{3+}$. This thus indicates spin bath is primarily comprised of impurity spins with a low g factor. Indeed we observe a broad ESR signal at 300–900 mT fields ($g = 1.3 - 0.4$), with peaks at $g = 0.71$ and $g = 0.81$ (Supplemental Material [36]). Impurity transitions at fields higher than 900 mT ($g = 0.4$) could not be measured due to the field limit of our magnet. Spins with $g = 0.4(0.7)$ are relatively unpolarized even at our lowest measurement temperature, with 87.1(98.1)%

polarization as compared to 99.996% polarization for the $^{167}\text{Er}^{3+}$ $g = 1.64$ transition around 259 mT. Therefore, the spectral diffusion measured is attributed to the unpolarized paramagnetic impurities within the host matrix.

B. Spectral diffusion at millikelvin temperatures

Next, we study the residual spectral diffusion at the lowest temperature of 26 mK to further validate our model of spectral diffusion. We use three-pulse echo (stimulated echo) technique with three $\pi/2$ pulses with a delay τ between the first and second pulses and a wait time T_W between the second and third pulses. For each value of T_W we sweep τ to measure the effective linewidth $\Gamma_{\text{eff}} = 1/(\pi T_2)$ [Fig. 3(b)],

$$\Gamma_{\text{eff}} = \Gamma_0 + \frac{1}{2}\Gamma_{\text{SD}}(1 - e^{-RT_w}), \quad (5)$$

where Γ_{SD} is spectral diffusion linewidth, R is total spin-flip rate, and Γ_0 is the linewidth in the absence of spectral diffusion [35,45].

We obtain Γ_{SD} of 64.5(8) kHz, R of 5.6(1.5) Hz and Γ_0 of 0.6(0.8) kHz at 26 mK. The fitted R and Γ_{SD} predict spectral diffusion limited coherence time ($T_{2,\text{SD}}$) of 1.87 ms from Eq. (3), which is in good agreement with the predicted $T_{2,\text{SD}}$ of 2.2 ms at 26 mK from the temperature-dependent spectral diffusion model. The total spin-flip rate R from three-pulse echo 5.6(1.5) Hz is higher than the measured 1.4(0.6) Hz spin-flip rate of $^{167}\text{Er}^{3+}$ $g = 1.64$ transition, further supporting the presence of paramagnetic impurity spins.

Close agreement between the spectral diffusion measurements from three-pulse echo and the temperature-dependence model substantiates our understanding of decoherence processes. Decreasing temperature lowers the spectral diffusion linewidth Γ_{SD} by a factor of $\text{sech}^2(g_{\text{env}}\mu_B B)/(2k_B T)$, and slows the total spin-flip rate R by freezing the direct phonon ($\coth(g_{\text{env}}\mu_B B)/(2k_B T)$) and flip-flop processes ($\text{sech}^2(g_{\text{env}}\mu_B B)/(2k_B T)$). The residual decoherence at 26 mK is dominated by slow spectral diffusion of approximately 5 Hz spin flips and a smaller contribution from instantaneous diffusion (Supplemental Material [36]).

To further investigate the spectral diffusion induced by paramagnetic impurities in Y_2O_3 , we perform pulsed ESR on a Y_2O_3 sample with no intentional erbium doping and observe spin-echo signals from impurity spins in the host matrix (Supplemental Material [36]). The T_2 measured on an impurity transition in undoped Y_2O_3 is comparable to T_2 measured in $^{167}\text{Er}^{3+}$ -doped Y_2O_3 at the same field, as expected. This also puts an upper limit on magnetic noise from flip flops of yttrium nuclear spins (δB_Y) as approximately equal to $1/(\pi g \mu_B T_2) = 9$ nT. The $^{167}\text{Er}^{3+}$ transition with 1.46 ms T_2 at 26 mK shows a nonexponential decay with a stretch factor of 2.1, indicating the

presence of a frozen core of yttrium nuclei in direct proximity to Er^{3+} with suppressed flip-flop dynamics [46,47]. While the estimated nuclear spin-bath limited T_2 based on yttrium density in Y_2O_3 is approximately equal to 1 ms [48], we can expect a longer T_2 due to the frozen core effect [3,47].

We note that the spin homogeneous linewidth deviates from linear dependence on temperature as expected in the case of magnetic two-level system (TLS) dominated decoherence in ceramics [23]. We observe a broad feature around $g \approx 2$, as well as a sharp $g = 1.97$ signal (F^+ defect center [49]) at high-temperature pulsed ESR, witnessing the presence of vacancy defects and magnetic TLS in the host matrix (Supplemental Material [36]). However, spins with $g \approx 2$ would be frozen with 99.9997% polarization at 26 mK and 259 mT, and are not expected to contribute significantly to spectral diffusion [10].

We also note that at 4 K, an isotopically purified $^{167}\text{Er}^{3+} : \text{Y}_2\text{O}_3$ sample exhibits up to 2800 times longer spin T_1 and up to 40 times longer spin T_2 compared to a natural abundance $\text{Er}^{3+} : \text{Y}_2\text{O}_3$ sample with same nominal doping, indicating an improvement of relaxation times with isotopic purification [20].

V. COHERENCE TIME ENHANCEMENT BEYOND SPECTRAL DIFFUSION

The spin-coherence time measurements for $g = 1.64$ transitions in Fig. 2(a) show instantaneous diffusion by dipolar interactions in the Er spin ensembles. This decoherence cannot be canceled by standard dynamical decoupling sequences like XY8. An alternative sequence is desired so that it can mitigate both spectral diffusion and dipolar interactions with robustness to pulse errors at the same time [50]. A previously proposed sequence for disorder-dominated sequence (Seq.B) has shown improvement over XY8 dynamical decoupling for electron spins in N-V centers [51] and Er:YSO [12]. These systems, however, have strong dipolar interactions with XY8 dynamically decoupled T_2 of the order of 1 μs as compared to T_2 of the order of ms in our system. For systems with weaker dipolar interactions, customized sequences are thus required. In this section, we describe the results of three customized sequences—CSeq1 for 3:1 (ratio between spectral diffusion and interaction decoupling), CSeq2 for 9:1, and CSeq3 for 12:1, together with existing XY8 (inf.:1) and Seq.B (6:1) on the 259 mT ($g = 1.64$) transition. We note that the ratio assigned to a sequence is how fast it decouples from slow-varying spectral diffusion noise versus dipolar-interaction-induced broadening, and it is an intrinsic property of the sequence. The actual ratio of spectral diffusion to dipolar interaction noise experienced by the spin system is difficult to predict when there is noise fluctuating faster than the sequence time scale. Therefore,

it is useful to design sequences with varying ratios to better match the actual noise characteristics of the system.

The starting point for the design of customized sequences is that a given sequence features different cycle lengths to mitigate either spectral diffusion or dipolar interactions by moving the system into a “Toggling Frame” [50], where we can obtain a pictorial visualization of how the original spin Pauli operators evolve under the Floquet-engineered version [52]. Figure 4(a) presents coherence time measurements for different sequences with the same 25-kHz filter center frequency. We observe that one customized sequence—CSeq2—outperforms all other sequences and even the XY8 sequence. All customized sequences yield longer coherence than Seq.B, with CSeq2 nearly reaching a factor of 2 improvement over Seq.B. We also note that when measuring Seq.B, spin-echo amplitudes quickly diminish below the noise floor after a few

data points. Therefore, only an upper limit of 1.6 ms is placed on Seq.B T_2 .

To understand the performance variations among difference sequences, we calculate their effective filter functions and compare with that of XY8 in Fig. 4(b). We also plot the noise power spectrum density (PSD) experienced by the system obtained by CPMG sequences with varying pulse separations (detailed information in the Supplemental Material [36]). While the dominant source of spectral diffusion is low-frequency noise with approximately Hz flip rate as discussed in Sec. IV, the noise PSD also exhibits a local maxima around 25 kHz. Compared with the XY8 sequence, the filter functions of the customized sequences generate sidebands that will sample less noises in total. We see from Fig. 4(b) that some customized sequences have wider sidebands than CSeq2 (i.e., CSeq1 and Seq.B) but do not outperform CSeq2 in terms of the coherence

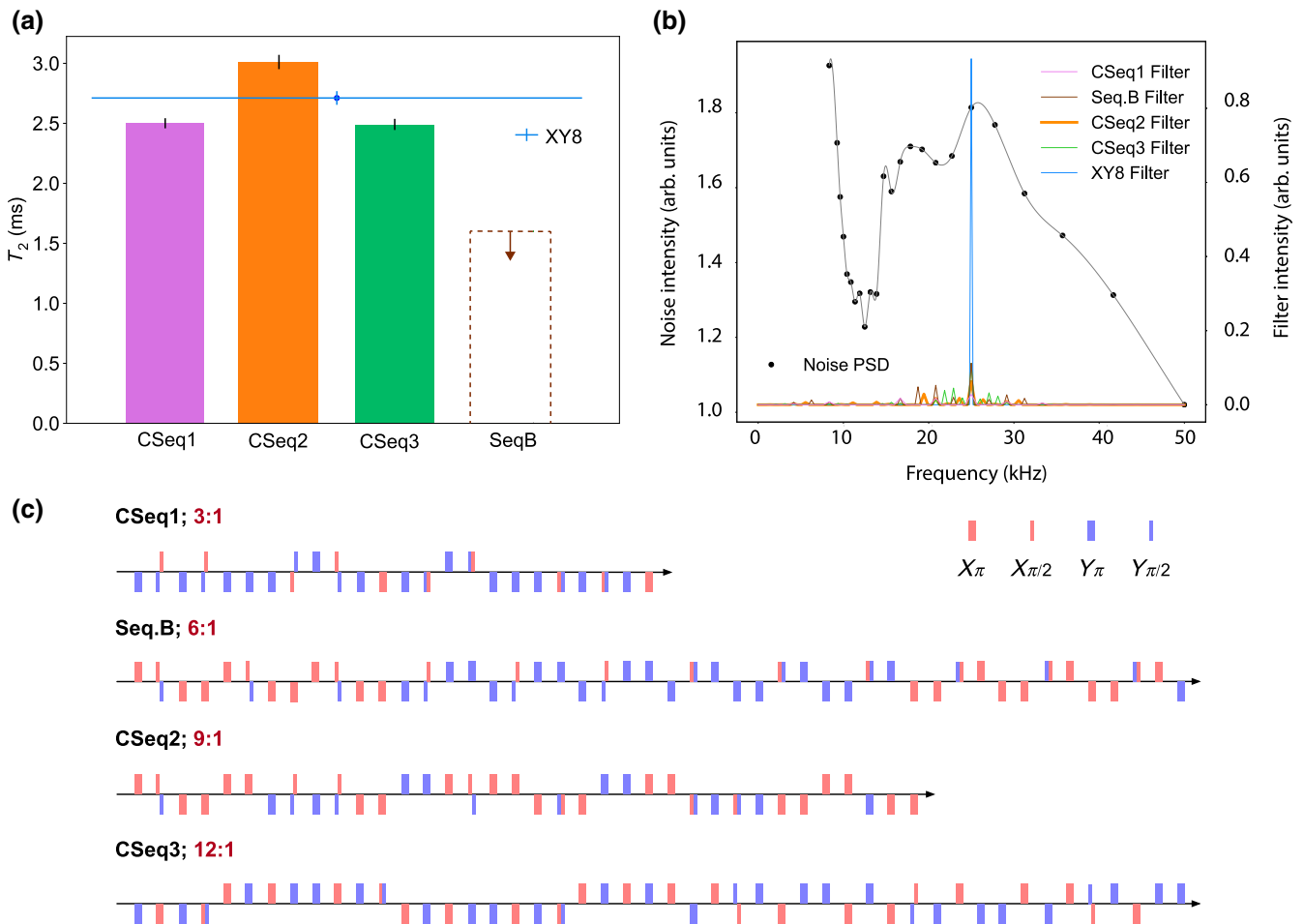


FIG. 4. Coherence enhancement with customized dynamical decoupling. (a) Comparison of coherence times under different dynamical decoupling sequences with a common 25-kHz filter center frequency. T_2 for Seq.B shown is an estimated upper bound. (b) Noise spectrum computed from CPMG T_2 measurement and comparison of the filter functions of all sequences. Filters are normalized in the whole spectrum but only the 0–50 kHz range is shown given the measured noise spectrum range. (c) Customized dynamical decoupling pulse sequences in increasing order of the target ratio of disorder to interaction, along with Seq.B.

time, indicating that the amount of dipolar interaction suppressed vary among different sequences and the coherence enhancement is not solely due to the spread of the filter function. Nonetheless, due to the fact that the electronic spin g tensor is highly anisotropic in Er^{3+} ions, customized sequences cannot fully cancel the dipolar interaction term in the spin Hamiltonian [12]. In this case, we can only tune the ratio between transverse (J_S) and longitudinal (J_L) coupling in the spin system by rearranging the pulse separations in the sequence, which give rise to relaxation and dissipation, respectively [51]. A longer coherence beyond current best result remains possible if such a ratio can be fine tuned. However, a full optimization is not performed in this work due to limitations of our experimental setup, such as the smallest accessible pulse width ($1 \mu\text{s}$) and the minimum pulse separation ($10 \mu\text{s}$).

VI. DISCUSSION

Our results show milliseconds erbium spin coherence is reliably achievable despite the presence of nuclear spins (e.g., yttrium) and paramagnetic impurities in the host matrix. To generalize, we obtain a long spin-coherence time by addressing low g -factor transitions and by freezing paramagnetic impurity spins at moderate fields and millikelvin temperatures. The remaining decoherence is attributed to unpolarized spins and dipolar interactions in the weakly interacting Er spin ensembles, which can be further mitigated by custom-designed dynamical decoupling sequence to simultaneously suppress spectral diffusion and dipolar interactions. This set of methods is generally applicable to erbium or other Kramers ions in wide-ranging hosts with low-site symmetries and anisotropic g tensors. According to Ref. [53], a plethora of crystalline hosts for Er in trigonal, tetragonal, monoclinic, and orthorhombic crystal-field symmetries exhibit the lowest g tensor component < 2 . A subset of them are also low-noise hosts with nuclear spin magnetic moments comparable or less than yttrium, such as CaWO_4 (tetragonal), SrWO_4 (tetragonal), ZnS (tetragonal), MgO (tetragonal), Si (monoclinic), Y_2SiO_5 (monoclinic) [48,53]. In these hosts, millisecond erbium spin-coherence times are expected following our strategy.

Our work along with a similar report in $^{167}\text{Er}^{3+}:\text{CaWO}_4$ [14] shows low g paramagnetic impurities as the dominant source of spectral diffusion in moderately doped ($\mathcal{O}(10)$ ppm) hosts at millikelvin temperatures. Reaching nuclear-spin-limited coherence times would require hosts with higher chemical purity and a very low concentration of paramagnetic dopants and defects on the order of ppb level [15]. In such highly dilute systems, the instantaneous diffusion limit is lifted, therefore spin coherence approaching the T_1 limit is expected after efficient dynamical decoupling of spectral diffusion noise. On the other hand, for dilute ensembles of rare-earth ions [$\mathcal{O}(10)$ ppm], either

dipolar interactions or paramagnetic impurities are likely the coherence-limiting factors, rather than nuclear spins. In those cases, hosts with a weak nuclear spins such as Y_2O_3 can provide coherence times on a par with nuclear spin-free hosts.

The polarized and reduced magnetic noise environment also indicates $^{167}\text{Er}^{3+}$ nuclear spin T_2 reaching a second is anticipated in Y_2O_3 at a similar field and temperature, which bodes well for high-fidelity long-term storage using nuclear-spin registers [54]. With the known hyperfine interactions [20], the $^{167}\text{Er}^{3+}$ nuclear spins can be initialized into one hyperfine level by sequential hyperpolarization via the Er electron spin, or via optical pumping [2]. This promising combination of long-lived electron-nuclear spins and strong hyperfine couplings will enable efficient quantum memories and multiqubit quantum nodes that are capable of remote entanglement generation and storage at the telecom band.

ACKNOWLEDGMENTS

We thank Tijana Rajh for useful discussions, and Ruoming Peng for valuable suggestions to the manuscript. This work is supported by National Science Foundation faculty early career development program (CAREER) Grant No. 1944715, the U.S. Department of Defense, Army Research Office grant no. W911NF2010296, the U.S. Department of Energy, Q-NEXT quantum science and engineering research center, and the NSF QLCI for Hybrid Quantum Architectures and Networks (NSF Grant No. 2016136).

-
- [1] C. Thiel, T. Böttger, and R. Cone, Rare-earth-doped materials for applications in quantum information storage and signal processing, *J. Lumin.* **131**, 353 (2011). [selected papers from DPC'10.](#)
 - [2] M. Rančić, M. P. Hedges, R. L. Ahlefeldt, and M. J. Sellars, Coherence time of over a second in a telecom-compatible quantum memory storage material, *Nat. Phys.* **14**, 50 (2018).
 - [3] M. Zhong, M. P. Hedges, R. L. Ahlefeldt, J. G. Bartholomew, S. E. Beavan, S. M. Wittig, J. J. Longdell, and M. J. Sellars, Optically addressable nuclear spins in a solid with a six-hour coherence time, *Nature* **517**, 177 (2015).
 - [4] G. Kurizki, P. Bertet, Y. Kubo, K. Mølmer, D. Petrosyan, P. Rabl, and J. Schmiedmayer, Quantum technologies with hybrid systems, *Proc. Nat. Acad. Sci.* **112**, 3866 (2015).
 - [5] H. J. Kimble, The quantum internet, *Nature* **453**, 1023 (2008).
 - [6] C. L. Degen, F. Reinhard, and P. Cappellaro, Quantum sensing, *Rev. Mod. Phys.* **89**, 035002 (2017).
 - [7] M. Raha, S. Chen, C. M. Phenicie, S. Ourari, A. M. Dibos, and J. D. Thompson, Optical quantum nondemolition measurement of a single rare earth ion qubit, *Nat. Commun.* **11**, 1605 (2020).

- [8] F. K. Asadi, S. C. Wein, and C. Simon, Protocols for long-distance quantum communication with single ^{167}Er ions, *Quantum Sci. Technol.* **5**, 045015 (2020).
- [9] M. Razavi, M. Piani, and N. Lütkenhaus, Quantum repeaters with imperfect memories: Cost and scalability, *Phys. Rev. A* **80**, 032301 (2009).
- [10] S. Probst, H. Rotzinger, A. V. Ustinov, and P. A. Bushev, Microwave multimode memory with an erbium spin ensemble, *Phys. Rev. B* **92**, 014421 (2015).
- [11] S. Welinski, P. J. T. Woodburn, N. Lauk, R. L. Cone, C. Simon, P. Goldner, and C. W. Thiel, Electron Spin Coherence in Optically Excited States of Rare-Earth Ions for Microwave to Optical Quantum Transducers, *Phys. Rev. Lett.* **122**, 247401 (2019).
- [12] B. Merkel, P. Cova Fariña, and A. Reiserer, Dynamical Decoupling of Spin Ensembles with Strong Anisotropic Interactions, *Phys. Rev. Lett.* **127**, 030501 (2021).
- [13] J.-Y. Huang, P.-Y. Li, Z.-Q. Zhou, C.-F. Li, and G.-C. Guo, Dynamical decoupling of spin ensembles with strong anisotropic interactions, *Phys. Rev. B* **105**, 245134 (2022).
- [14] M. Rančić, M. Le Dantec, S. Lin, S. Bertaina, T. Chanelière, D. Serrano, P. Goldner, R. B. Liu, E. Flurin, D. Estève, D. Vion, and P. Bertet, Electron-spin spectral diffusion in an erbium doped crystal at millikelvin temperatures, *Phys. Rev. B* **106**, 144412 (2022).
- [15] M. L. Dantec, M. Rančić, S. Lin, E. Billaud, V. Ranjan, D. Flanigan, S. Bertaina, T. Chanelière, P. Goldner, A. Erb, R. B. Liu, D. Estève, D. Vion, E. Flurin, and P. Bertet, Twenty-three-millisecond electron spin coherence of erbium ions in a natural-abundance crystal, *Sci. Adv.* **7**, eabj9786 (2021).
- [16] A. Ortu, A. Tiranov, S. Welinski, F. Fröwis, N. Gisin, A. Ferrier, P. Goldner, and M. Afzelius, Simultaneous coherence enhancement of optical and microwave transitions in solid-state electronic spins, *Nat. Mater.* **17**, 671 (2018).
- [17] J. V. Rakonjac, Y.-H. Chen, S. P. Horvath, and J. J. Longdell, Long spin coherence times in the ground state and in an optically excited state of $^{167}\text{Er}^{3+}$: Y_2SiO_5 at zero magnetic field, *Phys. Rev. B* **101**, 184430 (2020).
- [18] E. L. Hahn, Spin Echoes, *Phys. Rev.* **80**, 580 (1950).
- [19] S. Stoll and A. Schweiger, EasySpin, a comprehensive software package for spectral simulation and analysis in EPR, *J. Magn. Reson.* **178**, 42 (2006).
- [20] T. Rajh, L. Sun, S. Gupta, J. Yang, H. Zhang, and T. Zhong, Hyperfine interactions and coherent spin dynamics of isotopically purified $^{167}\text{Er}^{3+}$ in polycrystalline Y_2O_3 , *Mater. Quantum Technol.* **2**, 045002 (2022).
- [21] T. Zhong and P. Goldner, Emerging rare-earth doped material platforms for quantum nanophotonics, *Nanophotonics* **8**, 5821 (2019).
- [22] H. Zhang, J. Yang, S. Gray, J. A. Brown, T. D. Ketcham, D. E. Baker, A. Carapella, R. W. Davis, J. G. Arroyo, and D. A. Nolan, Transparent Er^{3+} -doped Y_2O_3 ceramics with long optical coherence lifetime, *ACS Omega* **2**, 3739 (2017).
- [23] R. Fukumori, Y. Huang, J. Yang, H. Zhang, and T. Zhong, Subkilohertz optical homogeneous linewidth and dephasing mechanisms in Er^{3+} : Y_2O_3 ceramics, *Phys. Rev. B* **101**, 214202 (2020).
- [24] T. L. Harris, *Erbium-based optical coherent transient correlator for the 1.5-micron communication bands*, Ph.D. thesis, MONTANA STATE UNIVERSITY (2001), provided by the SAO/NASA Astrophysics Data System.
- [25] G. D. Reinemer, *Optical characterization of perturbed sites and $C3i$ sites in rare earth doped oxide crystals*, Ph.D. thesis, Montana State University (2003), provided by the SAO/NASA Astrophysics Data System.
- [26] G. Schäfer and S. Scheller, Paramagnetische Resonanz von Er^{3+} in Y_2O_3 , *Phys. Kondens. Mater.* **5**, 48 (1966).
- [27] G. Schäfer, Paramagnetische Resonanz von Er^{3+} and Ce^{3+} in Y_2O_3 , *Phys. Kondens. Mater.* **9**, 359 (1969).
- [28] S. Probst, H. Rotzinger, S. Wunsch, P. Jung, M. Jerger, M. Siegel, A. V. Ustinov, and P. A. Bushev, Anisotropic Rare-Earth Spin Ensemble Strongly Coupled to a Superconducting Resonator, *Phys. Rev. Lett.* **110**, 157001 (2013).
- [29] J. S. Hyde, W. Froncisz, and T. Oles, Multipurpose loop-gap resonator, *J. Magn. Reson.* (1969) **82**, 223 (1989).
- [30] M. Šimėnas, J. O’Sullivan, C. W. Zollitsch, O. Kennedy, M. Seif-Eddine, I. Ritsch, M. Hülsmann, M. Qi, A. Godt, M. M. Roessler, G. Jeschke, and J. J. Morton, A sensitivity leap for X-band EPR using a probehead with a cryogenic preamplifier, *J. Magn. Reson.* **322**, 106876 (2021).
- [31] P.-Y. Li, C. Liu, Z.-Q. Zhou, X. Liu, T. Tu, T.-S. Yang, Z.-F. Li, Y. Ma, J. Hu, P.-J. Liang, X. Li, J.-Y. Huang, T.-X. Zhu, C.-F. Li, and G.-C. Guo, Hyperfine Structure and Coherent Dynamics of Rare-Earth Spins Explored with Electron-Nuclear Double Resonance at Subkelvin Temperatures, *Phys. Rev. Appl.* **13**, 024080 (2020).
- [32] M. Afzelius, C. Simon, H. de Riedmatten, and N. Gisin, Multimode quantum memory based on atomic frequency combs, *Phys. Rev. A* **79**, 052329 (2009).
- [33] Y. Ma, Y.-Z. Ma, Z.-Q. Zhou, C.-F. Li, and G.-C. Guo, One-hour coherent optical storage in an atomic frequency comb memory, *Nat. Commun.* **12**, 2381 (2021).
- [34] M. Businger, A. Tiranov, K. T. Kaczmarek, S. Welinski, Z. Zhang, A. Ferrier, P. Goldner, and M. Afzelius, Optical Spin-Wave Storage in a Solid-State Hybridized Electron-Nuclear Spin Ensemble, *Phys. Rev. Lett.* **124**, 053606 (2020).
- [35] H.-J. Lim, S. Welinski, A. Ferrier, P. Goldner, and J. J. L. Morton, Coherent spin dynamics of ytterbium ions in yttrium orthosilicate, *Phys. Rev. B* **97**, 064409 (2018).
- [36] See Supplemental Material at <http://link.aps.org/supplemental/10.1103/PhysRevApplied.19.044029> for details on ESR transition mixing calculation, instantaneous diffusion measurement, optical saturation of ESR, sample temperature calibration, spectral diffusion estimate, ESR signal from impurity and defects, custom sequence design and noise PSD extraction, Refs. [55–57].
- [37] B. Car, J.-L. Le Gouët, and T. Chanelière, Superhyperfine induced photon-echo collapse of erbium in Y_2SiO_5 , *Phys. Rev. B* **102**, 115119 (2020).
- [38] W. B. Mims, K. Nassau, and J. D. McGee, Spectral diffusion in electron resonance lines, *Phys. Rev.* **123**, 2059 (1961).
- [39] D. Suter and G. A. Álvarez, *Colloquium*: Protecting quantum information against environmental noise, *Rev. Mod. Phys.* **88**, 041001 (2016).
- [40] A. M. Souza, G. A. Álvarez, and D. Suter, Effects of time-reversal symmetry in dynamical decoupling, *Phys. Rev. A* **85**, 032306 (2012).
- [41] E. S. Petersen, A. M. Tyryshkin, K. M. Itoh, J. W. Ager, H. Riemann, N. V. Abrosimov, P. Becker, H. J. Pohl,

- M. L. W. Thewalt, and S. A. Lyon, Dynamical decoupling of interacting dipolar spin ensembles, (2018),.
- [42] K. W. Chan, W. Huang, C. H. Yang, J. C. C. Hwang, B. Hensen, T. Tanttu, F. E. Hudson, K. M. Itoh, A. Laucht, A. Morello, and A. S. Dzurak, Assessment of a Silicon Quantum Dot Spin Qubit Environment via Noise Spectroscopy, *Phys. Rev. Appl.* **10**, 044017 (2018).
- [43] J. R. Klauder and P. W. Anderson, Spectral diffusion decay in spin resonance experiments, *Phys. Rev.* **125**, 912 (1962).
- [44] T. Lutz, L. Veissier, C. W. Thiel, R. L. Cone, P. E. Barclay, and W. Tittel, Modification of phonon processes in nanostructured rare-earth-ion-doped crystals, *Phys. Rev. A* **94**, 013801 (2016).
- [45] T. Böttger, C. W. Thiel, Y. Sun, and R. L. Cone, Optical decoherence and spectral diffusion at 1.5 μm in $\text{Er}^{3+} : \text{Y}_2\text{SiO}_5$ versus magnetic field, temperature, and Er^{3+} concentration, *Phys. Rev. B* **73**, 075101 (2006).
- [46] J. Ganem, Y. P. Wang, D. Boye, R. S. Meltzer, W. M. Yen, and R. M. Macfarlane, Nonexponential Photon-Echo Decays of Paramagnetic Ions in the Superhyperfine Limit, *Phys. Rev. Lett.* **66**, 695 (1991).
- [47] N. Kukharchyk, D. Sholokhov, O. Morozov, S. L. Korabl-eva, A. A. Kalachev, and P. A. Bushev, Optical coherence of $^{166}\text{Er} : ^7\text{LiYF}_4$ crystal below 1 K, *New J. Phys.* **20**, 023044 (2018).
- [48] S. Kanai, F. J. Heremans, H. Seo, G. Wolfowicz, C. P. Anderson, S. E. Sullivan, M. Onizhuk, G. Galli, D. D. Awschalom, and H. Ohno, Generalized scaling of spin qubit coherence in over 12,000 host materials, *Proc. Nat. Acad. Sci.* **119**, e2121808119 (2022).
- [49] N. Kunkel, J. Bartholomew, L. Binet, A. Ikesue, and P. Goldner, High-resolution optical line width measurements as a material characterization tool, *J. Phys. Chem. C* **120**, 13725 (2016).
- [50] J. Choi, H. Zhou, H. S. Knowles, R. Landig, S. Choi, and M. D. Lukin, Robust Dynamic Hamiltonian Engineering of Many-Body Spin Systems, *Phys. Rev. X* **10**, 031002 (2020).
- [51] H. Zhou, J. Choi, S. Choi, R. Landig, A. M. Douglas, J. Isoya, F. Jelezko, S. Onoda, H. Sumiya, P. Cappellaro, H. S. Knowles, H. Park, and M. D. Lukin, Quantum Metrology with Strongly Interacting Spin Systems, *Phys. Rev. X* **10**, 031003 (2020).
- [52] U. Haeberlen and J. S. Waugh, Coherent averaging effects in magnetic resonance, *Phys. Rev.* **175**, 453 (1968).
- [53] C. A. J. Ammerlaan and I. de Maat-Gersdorf, Zeeman splitting factor of the Er^{3+} ion in a crystal field, *Appl. Magn. Reson.* **21**, 13 (2001).
- [54] A. Ruskuc, C.-J. Wu, J. Rochman, J. Choi, and A. Faraon, Nuclear spin-wave quantum register for a solid-state qubit, *Nature* **602**, 408 (2022).
- [55] C. Müller, J. H. Cole, and J. Lisenfeld, Towards understanding two-level-systems in amorphous solids: Insights from quantum circuits, *Rep. Prog. Phys.* **82**, 124501 (2019).
- [56] G. P. Dold, *milliKelvin ESR of rare-earth doped crystals using superconducting resonators*, Ph.D. thesis, UNIVERSITY COLLEGE LONDON (2020).
- [57] G. A. Álvarez and D. Suter, Measuring the Spectrum of Colored Noise by Dynamical Decoupling, *Phys. Rev. Lett.* **107**, 230501 (2011).